Chemical Engineering Journal 480 (2024) 148105

Contents lists available at ScienceDirect

Chemical Engineering Journal

journal homepage: www.elsevier.com/locate/cej

Enhanced lithiophilicity via bismuth-infused framework for advanced lithium metal batteries

Joo Hyeong Suh [a,1], Hamzeh Qutaish [b,1], Sang A Han [b], Gwang Hyeon Eom [a], Dong Ki Kim [a], Jong-Won Lee [c,*], Jung Ho Kim [b,*], Min-Sik Park [a,*]

[a] Department of Advanced Materials Engineering for Information and Electronics, Integrated Education Institute for Frontier Science & Technology (BK21 Four), Kyung Hee University, 1732 Deogyeong-daero, Giheung-gu, Yongin 17104, Republic of Korea

[b] Institute for Superconducting & Electronic Materials (ISEM), Australian Institute of Innovative Materials (AIIM), University of Wollongong, Innovation Campus, Squires Way, North Wollongong, NSW 2500, Australia

[c] Division of Materials Science and Engineering, Hanyang University, 222 Wangsimni-ro, Seongdong-gu, Seoul 04763, Republic of Korea

ARTICLE INFO

Keywords:
Li metal batteries
Porous structure
Zeolitic imidazolate framework
3D amorphous carbon
Galvanic displacement

ABSTRACT

Utilizing carbon materials as 3D lithium (Li) hosts hold a significant interest in constructing high-energy batteries. However, there are ongoing challenges associated with these frameworks owing to their poor Li affinity. Recent advancements, including alloying reactions with precious metals like silver (Ag) and gold (Au), have emerged as a promising technique to enhance the electrochemical performance of these host materials. Nevertheless, the search for cost-effective alternatives remains a pressing demand. Herein, this work employed galvanic displacement (GD) to integrate bismuth into disordered porous carbon (Bi-DPC) and optimized across different concentrations (0.01, 0.05, 0.1 M). As a result, the Li deposition onto the Bi-DPC surface exhibited dendrite-free planar morphologies, revealing an outstanding electrochemical performance, including a high CE of around 100 % over more than 100 cycles. These findings underscore the potential of Bi-infused porous carbon as a promising alternative for enhancing Li deposition processes.

1. Introduction

The utilization of lithium (Li) metals as anodes in batteries forms the bases of most energy storage devices [1–5]. This stems from the outstanding properties of Li as it can store high amounts of energy owing to its enormous theoretical specific capacity of 3860 mAh g^{-1}, low redox potential among the alkali metals (-3.04 V vs. standard hydrogen electrode), as well as its lightweight (0.53 g cm^{-3}) [6–10]. Despite these advantages, the use of Li metal anode comes with several limitations [11–15]. These encompass the formation of an uneven solid-electrolyte interphase (SEI), the growth of dendritic structures, the formation of dead Li, and the huge volume changes during Li plating and stripping processes [16–20]. These challenges give rise to critical concerns, including the potential for short-circuiting, diminished coulombic efficiency (CE), and a reduction in the overall battery capacity [21–24].

To address the challenges leading to the failure of Li metal batteries (LMBs), numerous researchers have explored different strategies to enhance the stability of the SEI [25–29]. These approaches include employing electrolyte additives [30,31], creating artificial SEI layers [32,33], and guiding Li deposition using three-dimensional (3D) porous frameworks [34,35]. Among these strategies, the latter technique has garnered significant interest recently. This is primarily due to its capability to accommodate the substantial volume changes that occur and to mitigate the effects of high local current density, ultimately leading to the suppression of dendritic growth. Zeolitic imidazolate framework-derived carbon (ZIF8-C) is one of the most promising candidates for cost-effective practical application of 3D-constructed porous hosts due to its outstanding properties [36], Studies found that for stable battery behavior, the most important property offered by ZIF8-C is the large surface area, as it reduces the local current density of the anode and prevents dendrite growth by modifying its lithiophilicity [37]. Furthermore, the pore network within ZIF8-C is highly electrochemically stable and can store a substantial amount of metallic Li while maintaining the electrode's structural integrity [38,39]. In addition, ZIF8-C exhibits robust mechanical strength that allows it to accommodate volume changes and resist internal stress [40,41].

* Corresponding authors.
E-mail addresses: jongwonlee@hanyang.ac.kr (J.-W. Lee), jhk@uow.edu.au (J.H. Kim), mspark@khu.ac.kr (M.-S. Park).
[1] Joo Hyeong Suh and Hamzeh Qutaish contributed equally to this work.

https://doi.org/10.1016/j.cej.2023.148105
Received 3 September 2023; Received in revised form 10 December 2023; Accepted 13 December 2023
Available online 16 December 2023

However, ZIF8-C is known for its microporous structure that hinders the deep penetration of Li ions into the internal pores, resulting in superficial plating at the surface and leaving the internal pores unutilized. While mesoporous structures have been previously adopted to facilitate Li-ion transport, upper surface electrodeposition could also result from the poor wettability of ZIF8-C, arising from the significant diffusion and nucleation barriers [42]. The low electrical conductivity is another drawback of ZIF8-C that results from its amorphous structure, limiting continuous electron transport and causing electrode polarization. While ZIF8-C can be functionalized with functional groups or heteroatoms, it is still challenging to attain a homogeneous Li electro-deposition.

Earlier studies demonstrated that alloying reactions with functional materials such as gold (Au) and silver (Ag) hold promise for stable Li plating [43–45]. Beyond their high costs, however, the tendency of these materials to aggregate easily can lead to pore clogging during the functionalization process [46–48]. Our strategic approach involves pioneering the use of bismuth (Bi) for the cost-effective synthesis of carbon-based host anodes. This is driven by its economic advantages and its higher availability compared to precious metals (as shown in Fig. S1 in the Supporting Information) [49]. Additionally, Bi exhibits considerable volumetric and theoretical capacities, coupled with a generous interlayer spacing (d = 3.95 Å), making it an ideal candidate for an alloying reaction with Li ions. This alloying capability effectively facilitates the accommodation of metallic Li [50–52].

Herein, our study involves the integration of Bi into mesoporous ZIF8-C, designated as disordered porous carbon (DPC), through the galvanic displacement (GD) process. The concentration of Bi was systematically varied and optimized within the range of 0.01 to 0.1 M to attain the most favourable electrochemical performance. Subsequently, the performance of the optimized Bi-DPC concentration was compared to that of standard DPC in terms of electrochemical Li storage capability and reversibility. The successful achievement of stable performance by utilizing Bi-DPC anodes establishes a pathway toward cost-effective, high-energy LMBs.

2. Experimental section

2.1. Synthesis of porous carbon from ZIF-8 (DPC)

A 50 ml solution (solution A) was prepared by mixing 2-methylimidazole (10 g, $C_4H_6N_2$, Sigma-Aldrich, 99 %) and SiO_2 (5 g, LUDOX TM-50, Sigma-Aldrich, 50 wt% suspension in H_2O) in deionized (DI) water. The blend was agitated at 300 rpm at 40 ℃. Another 50 ml solution (solution B) was created by dissolving zinc acetate (2 g, $Zn(CH_3COO)_2{\cdot}H_2O$, Sigma-Aldrich, 99 %) in DI water. Subsequently, solutions A and B were mixed and stirred for 10 min. During the overnight period, the mixture was allowed to stand at room temperature. This led to the formation of a white precipitate, which was collected after decanting the excess solution. Following this, 100 ml of methanol was added to the white precipitate and stirred overnight. It was then subjected to washing, using a solution containing ethanol and DI water in a 1:1 ratio. Subsequently, the precipitate was dried at 80 ℃ for 48 h. The resulting powder underwent carbonization at 900 ℃, using a heating rate of 5 ℃ min^{-1} for a duration of 6 h in an argon (Ar) setting. The obtained DPC was subsequently gathered and exposed to a 5 M solution of hydrofluoric acid (HF) for 1.5 h. Finally, the DPC underwent drying at 80 ℃ inside a vacuum oven throughout the night.

2.2. Functionalization of DPC

The Bi-DPC was prepared by the GD process. Three different concentrations were prepared: 0.01, 0.05, and 0.1 M using 0.73, 3.64, and 7.28 g of bismuth nitrate ($Bi(NO_3)_3{\cdot}5H_2O$, Sigma-Aldrich, 99 %) in 145 ml of DI water and 5 ml of nitric acid (HNO_3), respectively. The three mixtures were stirred continuously for 1 h. Following this, 0.5 g of the previously prepared DPC was introduced into the solution and agitated for 20 h at 50 ℃. Subsequently, the resulting Bi-DPC was washed with DI water and then dried at 80 ℃ within a vacuum oven overnight to activate it.

2.3. Structural characterizations

The microstructures and morphology of DPC and Bi-DPC were examined using transmission electron microscopy (TEM), energy dispersive X-ray spectroscopy (EDS), and field-emission scanning electron microscopy (FE-SEM). The chemical composition and crystal structure were explored using X-ray diffraction (XRD) employing monochromatic Cu Kα radiation (λ = 1.54056 Å), Raman spectroscopy, and X-ray photoelectron spectroscopy (XPS). The electrical characteristics of the materials were determined using a powder resistivity measurement setup. Furthermore, a porosity analyzer utilizing the Brunauer-Emmett-Teller (BET) method was employed to ascertain the total surface areas and pore volumes of the materials.

2.4. Electrochemical characterizations

To fabricate the electrodes, separate slurries were prepared using 80 wt% DPC and Bi-DPC, respectively, each combined with a conducting agent (Super P, 10 wt%) and a binder (polyvinylidene fluoride, PVdF, 10 wt%) in N-methyl-2-pyrrolidone (NMP). A copper (Cu) foil current collector served as the substrate for applying these slurries, followed by exposure to vacuum at 120 ℃ overnight. Following this, the cells were pressed at a pressure of 200 kg cm^{-2}. Li metal foil was utilized as the counter electrode in the construction of CR2032 coin-type cells. The separator consisted of a polyethylene (PE) membrane, while the electrolyte was created from 1 M lithium bis(trifluoromethanesulfonyl) imide (LiTFSI) in a mixture of dioxolane-dimethyl ether (DOL-DME; 50:50 by volume), with 1 wt% lithium nitrate ($LiNO_3$) included as an additive. Additionally, full cells were constructed using a commercially available $LiFePO_4$ (LFP) cathode with a theoretical capacity of 170 mAh g^{-1}, an active material loading of 4 mg cm^{-2}, and an areal capacity of 0.6 mAh cm^{-2}. We manufactured a full cell by integrating this cathode with a pre-stored Li anode with a capacity of 1.4 mAh cm^{-2}. The full cell was subjected to cycling under a constant current density of 0.2 mA cm^{-2}, within a voltage window ranging from 2.5 to 4.0 V.

3. Results and discussion

3.1. Material properties of Bi-DPC

The schematic illustration in Fig. 1 shows the Li plating behaviour on the DPC containing Zn, exhibiting a superficial deposition pattern with dendritic growth as opposed to the uniform Li plating within the Bi-DPC. In detail, the process starts from the early synthesis steps for DPC and Bi-DPC, as shown in Fig. 1a and S2. Herein, the mesoporous structures were obtained after etching SiO_2 using HF, resulting in open pathways that facilitate the diffusion of Li ions. For Bi-DPC, spontaneous GD reactions of Zn via Bi occurred by the disparity in the reduction potential difference between the Bi and Zn metals. The relatively lower formation energy value between Li and Bi creates favourable deposition sites for Li plating, in contrast to the higher formation energy between Li and Zn (Fig. 1c). This is further confirmed by the SEM images in Fig. 1b,d, which distinctively show dendritic Li growth for DPC and smooth Li deposition for Bi-DPC. For a comprehensive comparison, we studied the material properties and deposition characteristics of our developed Bi-DPC across various concentrations (0.01Bi-DPC, 0.05Bi-DPC, and 0.1Bi-DPC) and compared them with those of pristine DPC as a reference.

Fig. 2a-c presents SEM and TEM images demonstrating the overall morphology of rhombic dodecahedral particles with an average size of 500 nm for Bi-DPC at varying concentrations. Similar size and morphology characteristics are also evident for DPC, which are further elucidated in Fig. S3a-b. Fig. S3 provides invaluable insights into the

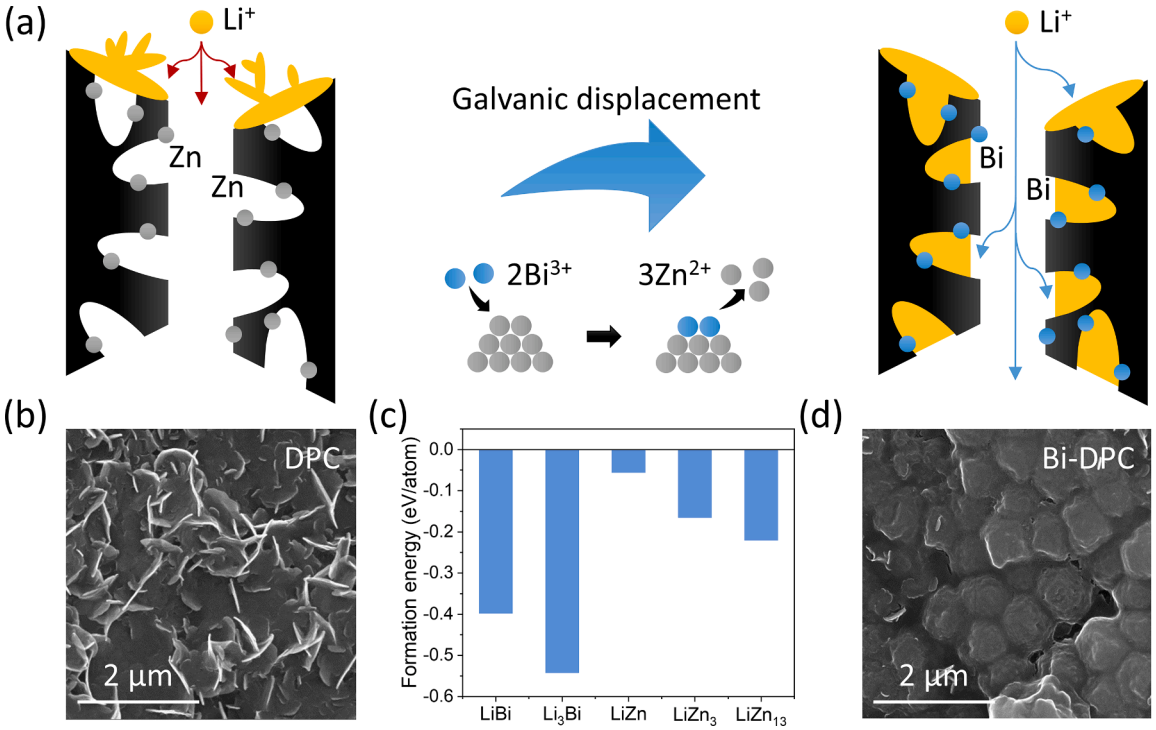

Fig. 1. (a) Schematic illustration demonstrating the impact of Bi on Li deposition within the mesoporous structures compared to zinc-containing derived mesoporous carbon (DPC). The SEM images at the bottom show the difference between Li growth patterns on (b) DPC (dendritic growth) and (d) Bi-DPC (axial growth). (c) The formation energy was carried out using data from the Materials Project database, indicating improved Li affinity in the context of the alloying reaction involving Bi.

composition of DPC, underlining the even distribution of Zn particles within the main amorphous carbon framework. Furthermore, the effectiveness of the GD process is evidenced by the substitution of Bi for Zn at different concentrations in a uniformly distributed manner. This uniform dispersion holds significance, as the consistent distribution of the functional material dictates the homogeneity of the Li-ion flux during cycling. Additionally, the EDS elemental mappings show elevated Bi intensities (color-coded in red) in 0.1Bi-DPC, as anticipated when compared to 0.05Bi-DPC and 0.01Bi-DPC. Interestingly, the nitrogen intensity in 0.1Bi-DPC is relatively stronger than that of others. To confirm the effect of metal and nitrogen content on the electrical conductivity, powder resistivity analysis was conducted on DPC and different Bi-DPC concentrations under different applied pressures from 5 to 20 kN (Fig. S4). It was shown that the electrical conductivity of 0.1Bi-DPC is the highest among all concentrations and three orders of magnitude higher than DPC. The electrical conductivity of 0.1Bi-DPC increased linearly with pressure from 3.4 S cm^{-1} at 5 kN to 16.1 S cm^{-1} at 20 kN.

The XRD patterns presented in Fig. 3a show broad peaks at low Bragg angles that are correlated with the amorphous carbon nature of DPC, 0.01Bi-DPC, 0.05Bi-DPC, and 0.1Bi-DPC. Additionally, characteristic peaks corresponding to the metallic Bi are evident in 0.05Bi-DPC and 0.1Bi-DPC. Among these, the most significant characteristic peaks appear in 0.1Bi-DPC, whereas 0.01Bi-DPC shows little or no presence of metallic peaks due to the low Bi concentration. In detail, the most significant diffraction peaks, especially (0 1 2) at $2\theta = 27°$, are attributed to the presence of bismuth. Upon comparing all the results, we conclude that the visibility of low-intensity reflections such as (0 0 3), (1 0 1), and (0 1 8) suggests that the relative amount of Bi in the 0.1Bi-DPC sample is higher than in the other samples. The substitution of Bi for Zn is confirmed by the calculated Bi/Zn ratios obtained from the EDS elemental mapping results, showing an increase from 14.1 % for 0.01Bi-DPC to 66.1 % for 0.1Bi-DPC, as presented in Fig. 3b. Further validation of the amorphous nature of Bi-DPC is found in the Raman spectra shown for the three Bi-DPC concentrations and DPC, as shown in Fig. 3c. This implies that the GD process has no impact on the structure of the DPC. In detail, the appearance of peaks at 1328 and 1584 cm^{-1}, associated with the G- and D-bands respectively, reveals the presence of both disorganized carbon and graphitic carbon structures. The relative peak intensity ratio of the D band to the G band, represented by I_D/I_G, was determined to be approximately 1.05, indicating a high presence of defects within the structure of DPC.

The N_2 adsorption–desorption measurements demonstrate typical type-IV isotherms, and the corresponding pore size distributions are compared in Fig. 3d-e, reflecting the size of the previously etched SiO_2 and confirming the design of the mesopores. The specific surface areas and pore volumes of Bi-DPC, as illustrated in Fig. 3f, show negligible changes when compared to DPC. This indicates that the desired mesoporous structure is maintained for facilitating Li-ion transport. Increasing the Bi concentration beyond a certain limit can certainly affect the size of Bi particles and hence clog the pore structures. However, the chosen concentrations in this study did not cause any direct effect on the pore volume but rather on the Li deposition behavior. More specifically, the pore volume was calculated to be 0.53, 0.56, 0.51, and 0.52 $cm^3\ g^{-1}$, and the BET surface area was determined to be 710, 692, 673, and 657 $m^2\ g^{-1}$ for DPC, 0.01Bi-DPC, 0.05Bi-DPC, and 0.1Bi-DPC, respectively.

3.2. *Electrochemical performance of Bi-DPC*

3.2.1. *The effect of Bi concentrations*

We examined the electrochemical performance of Bi-DPC at various concentrations and compared it to that of the DPC as a reference. Galvanostatic cycling was conducted in half-cells to identify the concentration that provides optimal reversibility and Li storage capability. An interesting observation is the inverse correlation between nucleation the overpotential and the Bi concentration, as shown in Fig. 4a-b. The cycling performance was measured at a current density of 0.2 mA cm^{-2} and an areal capacity of 0.2 mAh cm^{-2} (Fig. 4c). In the case of 0.01Bi-DPC and 0.1Bi-DPC anodes, stable cyclability was sustained for

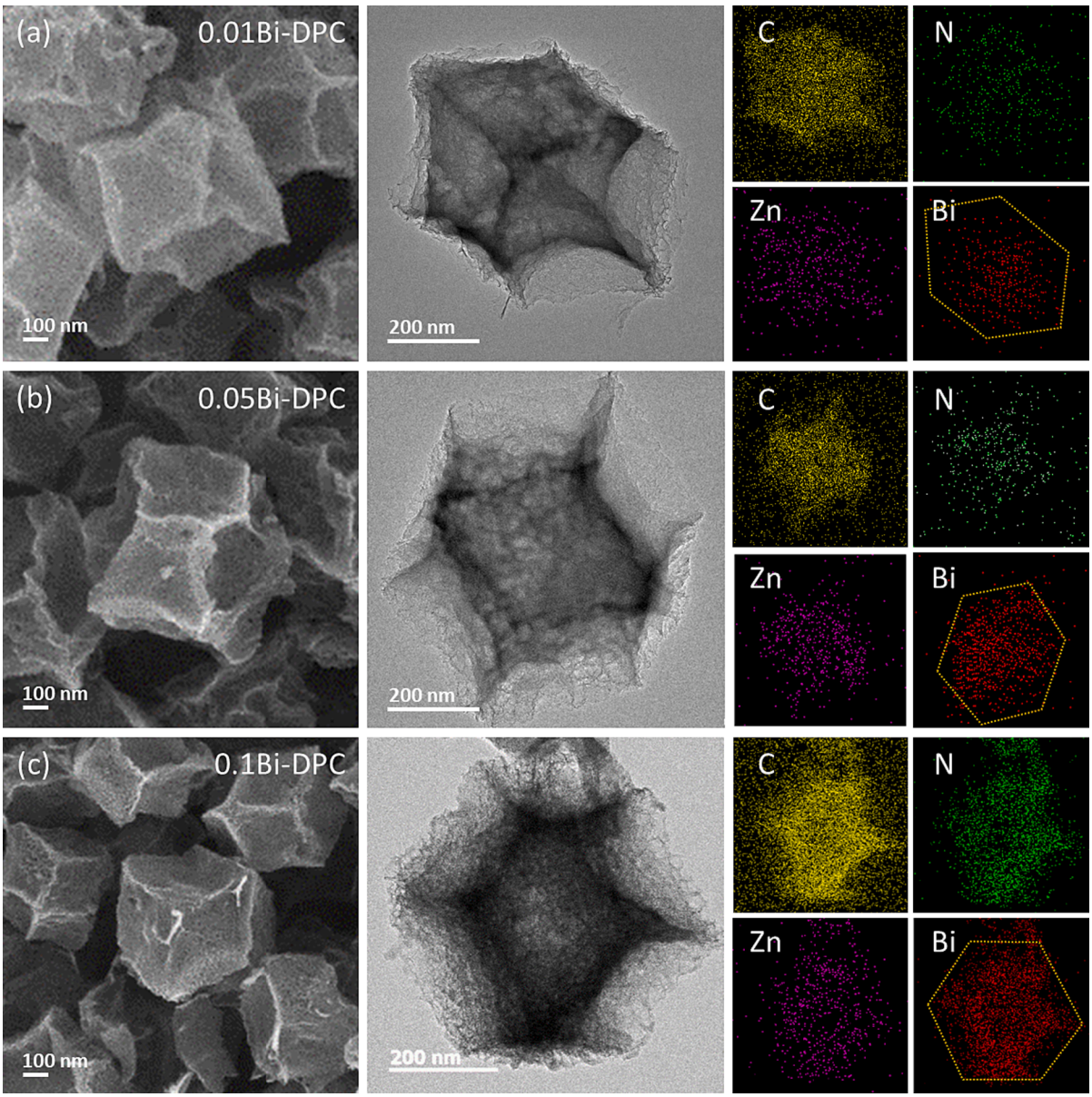

Fig. 2. SEM images, TEM images, and EDS elemental mappings of (a) 0.01Bi-DPC, (b) 0.05Bi-DPC, and (c) 0.1Bi-DPC.

approximately 120 and 160 h, respectively, after which, a noticeable increase in overpotential occurred. Conversely, the 0.05Bi-DPC anode showed the most stable cyclability over 200 h with the least overpotential. In contrast, the DPC anodes exhibited a significant overpotential after around 60 h of cycling, indicating the accumulation of inactive or dead Li. The rate capability was also evaluated at the different current densities of 0.2, 0.5, and 1 mA cm^{-2}, before returning to the initial value of 0.2 mA cm^{-2}, as shown in Fig. 4d. Note that the samples with all three Bi concentrations and DPC demonstrate excellent rate capabilities with negligible change. A slightly larger voltage gap appeared in DPC, 0.01Bi-DPC, and 0.1Bi-DPC compared to 0.05Bi-DPC at 1 mA cm^{-2}.

In order to understand and evaluate the performances of Bi-DPC for practical usage of Li-metal battery applications, a pouch cell with a layered design has been employed to allow maximum use of space and active materials. Fig. 4e shows the pouched cell performance at a current density of 4 mA cm^{-2}. The cycle test revealed that while DPC exhibited internal shorting before reaching 200 h, 0.05Bi-DPC demonstrated a stable and uniform voltage profile without significant overpotentials for over 250 h.

The performance of full-cells was also assessed at different Bi concentrations and compared to that of the DPC. A commercially available $LiFePO_4$ (LFP) was used as a cathode, functioning within a voltage range of 2.5 to 4.0 V. Fig. 5a shows the galvanostatic charge–discharge profiles for the first cycle of full-cells employing DPC, 0.01Bi-DPC, 0.05Bi-DPC, and 0.1Bi-DPC anodes. Among the different concentrations, the full-cell with 0.05Bi-DPC anode showed the highest discharge specific capacity of approximately 150 mAh g^{-1}, indicating superior Li-ion accessibility. As indicated by the Nyquist plots in Fig. 5b, all the full-cells employing 0.01Bi-DPC, 0.05Bi-DPC, and 0.1Bi-DPC anodes exhibited significantly reduced charge transfer resistance (R_{ct}) of 37.8, 34.3, and 44.2 Ω, respectively, compared to DPC (72.0 Ω). This reduction is mainly attributed to the fast Li ion transport and strong Li-host interaction facilitated by the galvanically displaced Bi, especially in the case of 0.05Bi-DPC [53]. Fig. 5c shows the cycling performances for the full-cells configured with Bi-DPC anodes with varying Bi concentrations at an areal capacity of 0.6 mAh cm^{-2} and a constant current density of 0.2 mA cm^{-2} for 100 cycles. It was found that the specific capacity of the LFP || DPC and LFP || 0.1Bi-DPC full-cells was notably decreased from 144.8 to 84.9 mAh g^{-1} and from 158.5 to 113.1 mAh g^{-1} with a capacity

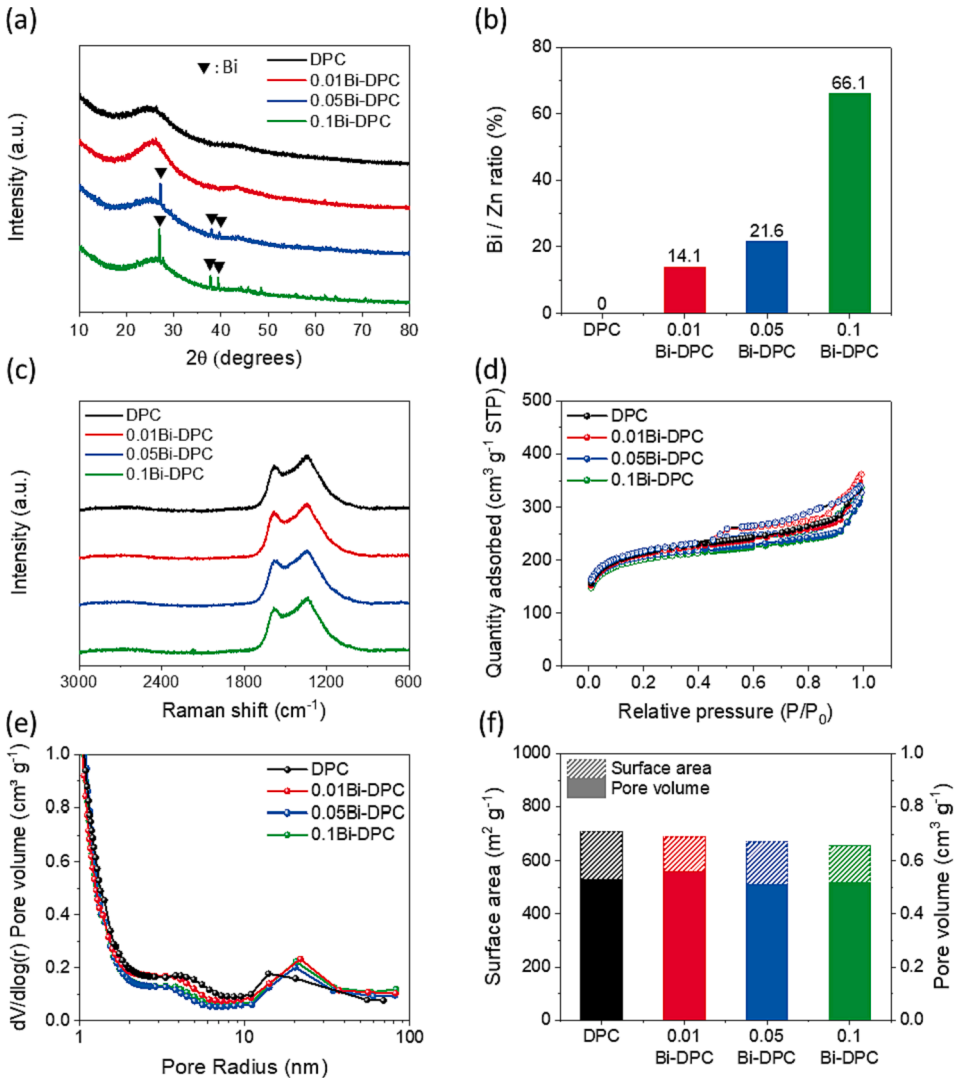

Fig. 3. Comparative analysis of Bi-DPC at different concentrations and DPC based on (a) XRD patterns, (b) Bi/Zn atomic ratios, (c) Raman spectra, (d) N_2 adsorption–desorption isotherms, (e) pore size distributions, and (f) surface areas and pore volumes.

retention of around 58.6 % and 71.4 % after 100 cycles, respectively. On the contrary, the LFP || 0.05Bi-DPC and LFP || 0.01Bi-DPC cells showed a relatively slower decrease in the specific capacity, with both maintaining a capacity retention of around 81.7 %. Furthermore, all full-cells with Bi-DPC anodes showed stable Coulombic efficiency (CE) of almost 100 % over the 100 cycles. In the case of LFP || DPC, however, some disruption in CE was observed after only 40 cycles. The rate capabilities of all the full-cells with Bi-DPC anodes (see Fig. S5a-b) demonstrated relatively stable performance, with slightly higher specific capacity in the case of the full-cell with 0.05Bi-DPC anode at all applied current densities.

For a comprehensive insight into the performance degradation, we acquired incremental capacity curves. By plotting differential voltage (*dQ/dV*) curves, it became evident that the full-cell with DPC anode gradually undergoes a phase shift and a detrimental decrease in capacity, corresponding to the capacity fading (Fig. 5d). In contrast, the full-cell with the best performing 0.05Bi-DPC anode demonstrated a relatively smaller phase shift. Additionally, the area under the curves remained consistent across 100 cycles, demonstrating superior stability and reversibility for Li plating and stripping (Fig. 5e).

The electrochemical properties of Bi-DPC at various concentrations were further verified through the Li deposition behavior on the anode surface, as illustrated in Fig. S6. In detail, the high or abundant amount of Bi in 0.1Bi-DPC causes preferential Li growth on the closest superficial Bi particles rather than within the mesoporous pathways, resulting in dendritic growth of metallic Li. Similarly, the low amount of Bi in 0.01Bi-DPC results in uneven Li growth, which is attributed to the widely dispersed Bi particles and results in limited wettability towards Li. The optimal performance of 0.05Bi-DPC, on the other hand, is owing to the fact that the well-calibrated distribution and quantity of Bi particles facilitate uniform Li deposition inside the porous structure of Bi-DPC and onto the anode surface. The significant differences in these concentrations were further confirmed by examining the SEM images of the electrode surface after 100 cycles (Fig. S6b) and the TEM images of particle morphology after initial plating (Fig. S6c). Our literature survey showed how our electrochemical performance compare to other published work (Table 1).

Fig. 6 illustrates the crucial role of Bi within a porous carbon host during the Li deposition process. Previous studies indicate that introducing metals is capable of forming alloys with Li and it becomes possible to deposit Li selectively at specific sites while maintaining a high lithium affinity. Particularly, when Ag particles reside within the porous host, Li deposition occurs from the inside towards the surface due to Li's strong affinity with Ag. However, Ag has the disadvantage of cost inefficiency and particle aggregation tendency during galvanic replacement due to its high surface energy. (Fig. S7) This can cause a

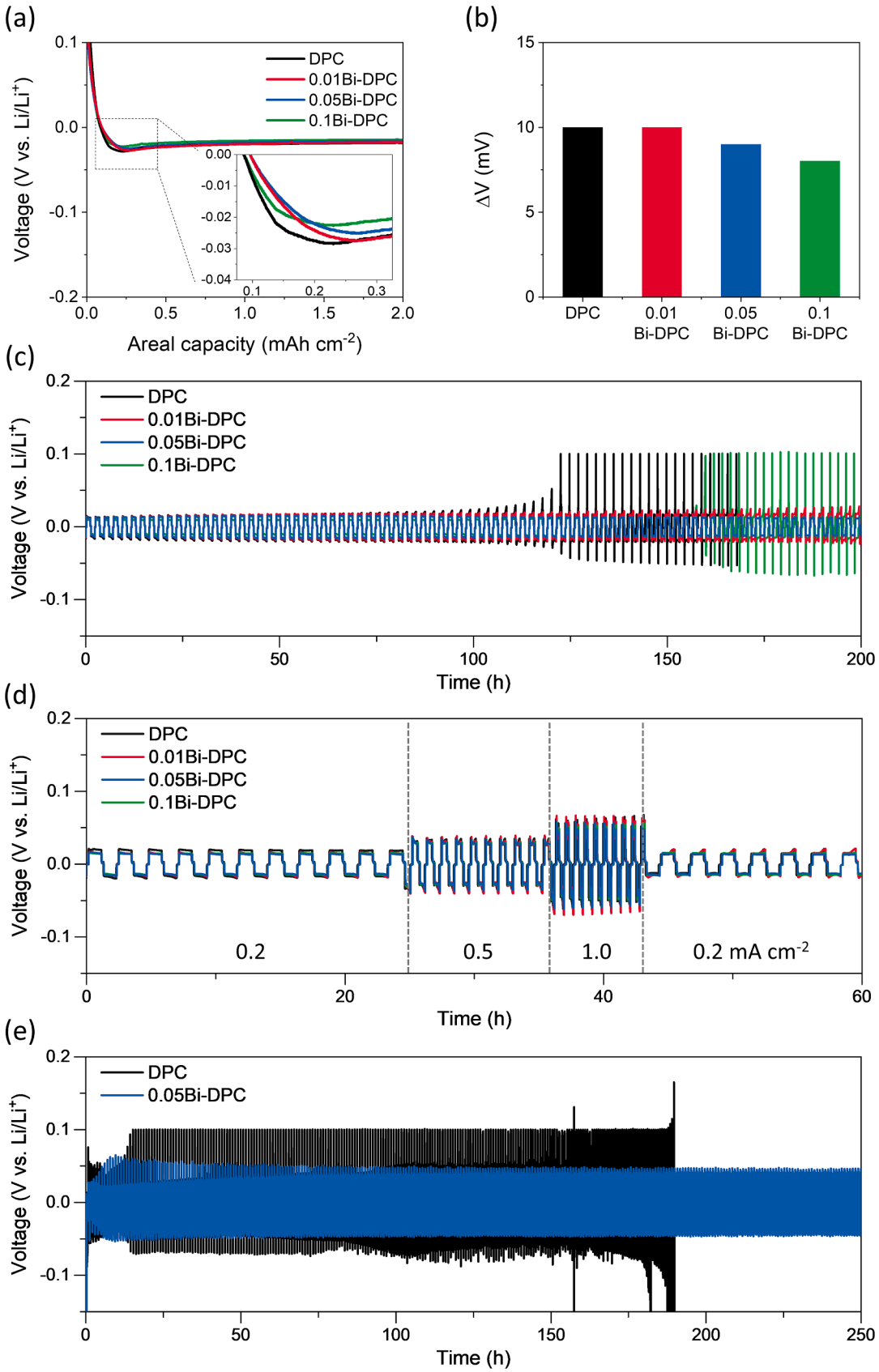

Fig. 4. Electrochemical performance comparison of Bi-DPC at different concentrations with standard DPC regarding (a) and (b) the nucleation overpotentials, (c) the voltage profiles at a current density of 0.2 mA cm^{-2} and an areal capacity of 0.2 mAh cm^{-2}, and (d) the rate capabilities. (e) The voltage profiles of the pouch cell at a current density of 4 mA cm^{-2} and an areal capacity of 1.1 mAh cm^{-2}.

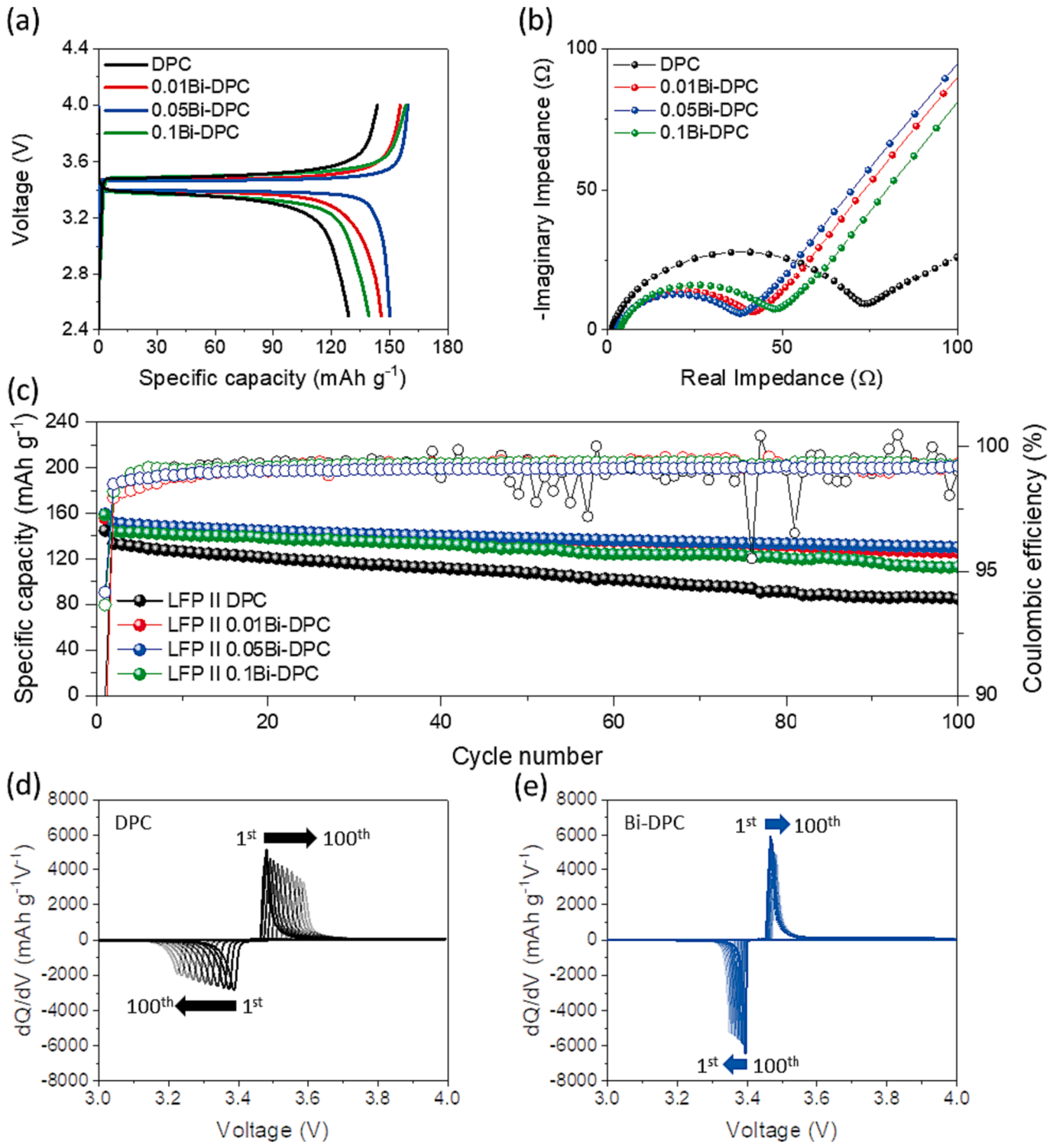

Fig. 5. Full-cell electrochemical performance of Bi-DPC at different concentrations and standard DPC: (a) galvanostatic voltage profiles at a current density of 0.2 mA cm^{-2}, (b) Nyquist plots, (c) cycling performances and Coulombic efficiencies at a current density of 0.2 mA cm^{-2}. (d) and (e) differential voltage (*dQ/dV*) curves of 0.05Bi-DPC recorded at every 10th cycle over 100 cycles at a current density of 0.2 mA cm^{-2}.

challenge over repeated cycles of Li plating and stripping, leading to localized Li deposition. In contrast, the introduction of Bi within the porous carbon host results in even dispersion without particle agglomeration post galvanic displacement. These characteristic positions Bi as a superior alternative to Ag, outperforming in terms of both cost-effectiveness and efficiency. To further support these findings, the corresponding TEM observation was carried out. In contrast to DPC (Fig. 6a), Bi-DPC reveals a smooth Li deposition within the host structure, as demonstrated in both the schematic and TEM images provided in Fig. 6b.

3.2.2. *Reaction mechanism of Bi-DPC*

To further investigate the reaction mechanism of Bi-DPC, we performed cyclic voltammetry (CV) on 0.05Bi-DPC, referred to as Bi-DPC

Table 1
Electrochemical performances of Li-metal anodes utilizing carbon-based nanocomposite frameworks. NPs stands for nanoparticles.

Material	Li nucleation overpotential (mV)	Current density (mA cm^{-2})	CE (%)	Cycle (h)	Areal capacity (mAh cm^{-2})	Ref.
Bi-DPC	8.0	4.0	100	250	1.1	This work
Ag/N-porous carbon	–	1.0	98	800	1.0	[44]
Au/hollow carbon	–	0.5	98	300	1.0	[46]
MnO/N-porous carbon	–	1.0	97	200	1.0	[54]
ZnO-porous carbon	40.0	1.0	97	200	1.0	[55]

hereafter, with a scan rate of 0.1 mV s^{-1}, as shown in Fig. 7a [56]. During the cathodic scan (Li plating), the first reduction peak was observed at 0.76 V, which corresponds to the alloying reaction of Bi with Li to form the intermediate LiBi phase. Subsequently, a second peak was found at 0.7 V vs. Li/Li^+, signifying the formation of Li_3Bi phase. In the anodic scan (Li stripping), a distinct oxidation peak was observed at 0.89 V vs. Li/Li^+, indicating the reversible dealloying process for Li_3Bi. The behavior shown in the electrochemical reactions agreed with the XPS analysis (see Fig. 7b), which shows the chemical evolution of Bi in the Bi-DPC at selected states of charge. Before Li plating, the Bi $4f_{7/2}$ and Bi $4f_{5/2}$ peaks were observed at around 159.0 and 164.1 eV, respectively. The CV curve indicates that the first reduction reaction takes place at 0.76 vs. Li/Li^+, which was confirmed by the XPS through a slight shift in the Bi $4f_{7/2}$ and Bi $4f_{5/2}$ peaks to lower binding energies of 158.7 and 163.8 eV, respectively, indicating the formation of the intermediate LiBi phase. Upon Li plating to 0.7 V vs. Li/Li^+, more pronounced peak shifts were observed in the spectrum of the Bi-DPC compared to the DPC, reflecting the formation of Li_3Bi phase. During the Li stripping at 0.8 V vs. Li/Li^+, however, the binding energies of Bi $4f_{7/2}$ and Bi $4f_{5/2}$ peaks reverted to their original values with only slight variation, elucidating the dealloying reaction of Li_3Bi phase. Hence, it was concluded that the alloying and dealloying behavior of Bi-DPC remains remarkably reversible during the long-term cycling process, which aligns well with our previous findings on stable cycling in the electrochemical evaluation. In addition, utilizing a nitrate-based precursor in the galvanic displacement process not only facilitates the substitution of Bi but also allows for the functionalization of the DPC with oxidized nitrogen groups. This functionalization of the carbon surface with oxidized nitrogen during lithium plating and stripping catalyzes the formation of lithium nitride (Li_3N) within the solid electrolyte interphase (SEI), which in turn significantly enhances the surface morphology of lithium deposition. Actual XPS analysis results confirm an increase in oxidized nitrogen content after the galvanic displacement process, and an increased content of Li_3N after cycling (Fig. S8). These changes contribute to the stabilization of the SEI film, as nitrogen's lone pair electrons facilitate Li^+ mass transfer and the conversion into the Li_3N phase during the initial discharge process is instrumental in this stabilization.

4. Conclusion

The challenges associated with using DPC as Li host materials have led to an exploration of innovative solutions. This study demonstrated a promising way to mitigate dendritic Li growth through a highly-efficient and cost-effective approach. By incorporating Bi into the DPC host using GD process, we optimized the Bi concentration to achieve optimal electrochemical performance of Bi-DPC anode for use in LMBs. The Bi-DPC consistently maintained its performance and structural integrity. This study leverages the unique properties of Bi-based anodes and provides expanding opportunities to improve Li deposition. Our work is expected to offer a perspective on the understanding of the enhancing electrochemical performance, as well as provide a fundamental framework for designing anodic Bi-DPC materials with high-performance. Due

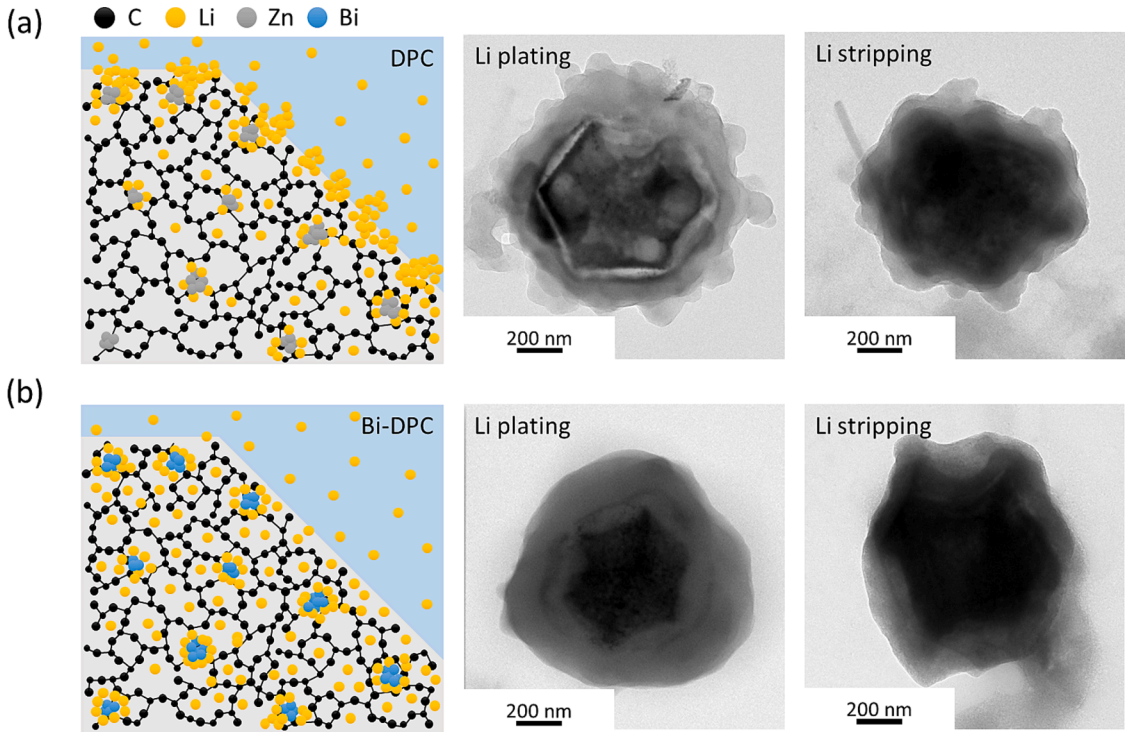

Fig. 6. Schematic illustrations and TEM images confirming the morphology of Li deposition: (a) in the DPC, and (b) in the Bi-DPC after 100 cycles.

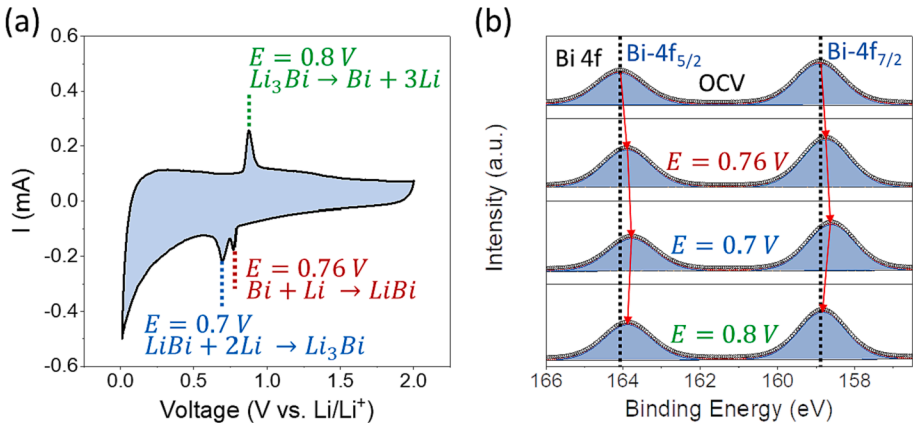

Fig. 7. (a) Cyclic voltammogram of 0.05Bi-DPC recorded with a scan rate of 0.1 mV s^{-1}, (b) XPS analysis of the Bi spectra revealing the chemical evolution during the Li plating and stripping.

to the complexity of understanding the Li adsorption and the various factors that can influence the electrochemical performance of the Bi-DPC, however, additional scientific exploration is necessary. Especially utilizing molecular dynamic simulations of the electrodes and phase-field simulations of local lithium adsorption processes.

CRediT authorship contribution statement

Joo Hyeong Suh: Conceptualization, Investigation, Methodology. **Hamzeh Qutaish:** Conceptualization, Formal analysis, Investigation, Methodology, Writing – original draft. **Sang A Han:** Data curation, Validation, Visualization, Writing – original draft. **Gwang Hyeon Eom:** Data curation, Investigation. **Dong Ki Kim:** Data curation, Investigation. **Jong-Won Lee:** Methodology, Writing – review & editing. **Jung Ho Kim:** Supervision, Visualization, Writing - original draft, Writing - review & editing. **Min-Sik Park:** Conceptualization, Funding acquisition, Methodology, Project administration, Writing – original draft, Writing – review & editing.

Declaration of competing interest

The authors declare that they have no known competing financial interests or personal relationships that could have appeared to influence the work reported in this paper.

Data availability

No data was used for the research described in the article.

Acknowledgements

This work was supported by the National Research Foundation (NRF-2021M1A2A2038143 and NRF-2018R1A5A1025594) of the Ministry of Science and ICT of the Republic of Korea.

Appendix A. Supplementary data

Supplementary data to this article can be found online at https://doi.org/10.1016/j.cej.2023.148105.

References

[1] J.H. Kim, Grand challenges and opportunities in batteries and electrochemistry, Front. Batter. Electrochem. 1 (2022) 1066276, https://doi.org/10.3389/fbael.2022.1066276.
[2] Z. Hou, S. Xia, C. Niu, Y. Pang, H. Sun, Z. Li, Y. Xu, S. Zheng, Tailoring the interaction of covalent organic framework with the polyether matrix toward high-performance solid-state lithium metal batteries, Carbon Energy 4 (2022) 506–516, https://doi.org/10.1002/cey2.190.
[3] Y. Fan, X. He, H. Li, Y. Huang, C. Sun, H. Liu, E. Huangzhang, F. Sun, X. Zhao, J. Nan, Lithiophilic Ni3S2 layer decorated nickel foam (Ni3S2@Ni foam) with fast ion transfer kinetics for long-life lithium metal anodes, Chem. Eng. J. 450 (4) (2022), 138384, https://doi.org/10.1016/j.cej.2022.138384.
[4] R. Pathak, K. Chen, F. Wu, A.U. Mane, R.V. Bugga, J.W. Elam, Q. Qiao, Y. Zhou, Advanced strategies for the development of porous carbon as a Li host/current collector for lithium metal batteries, Energy Storage Mater. 41 (2021) 448–465, https://doi.org/10.1016/j.ensm.2021.06.015.
[5] D.T. Boyle, X. Kong, A. Pei, P.E. Rudnicki, F. Shi, W. Huang, Z. Bao, J. Qin, Y. Cui, Transient voltammetry with ultramicroelectrodes reveals the electron transfer kinetics of lithium metal anodes, ACS Energy Lett. 5 (2020) 701–709, https://doi.org/10.1021/acsenergylett.0c00031.
[6] H. Qutaish, S.A. Han, Y. Rehman, K. Konstantinov, M.-S. Park, J.H. Kim, Porous carbon architectures with different dimensionalities for lithium metal storage, Sci. Technol. Adv. Mater. 23 (1) (2022) 169–188, https://doi.org/10.1080/14686996.2022.2050297.
[7] J. Liu, Z. Bao, Y. Cui, E.J. Dufek, J.B. Goodenough, P. Khalifah, Q. Li, B.Y. Liaw, P. Liu, A. Manthiram, Y.S. Meng, V.R. Subramanian, M.F. Toney, V. V. Viswanathan, M.S. Whittingham, J. Xiao, W. Xu, J. Yang, X.-Q. Yang, J.-G. Zhang, Pathways for practical high-energy long-cycling lithium metal batteries, Nat. Energy 4 (3) (2019) 180–186, https://doi.org/10.1038/s41560-019-0338-x.
[8] M.-S. Park, J.H. Kim, Salt-philic and solvent-phobic, Nat. Energy 8 (6) (2023) 558–559, https://doi.org/10.1038/s41560-023-01257-0.
[9] D. Lin, Y. Liu, Y. Cui, Reviving the lithium metal anode for high-energy batteries, Nat. Nanotechnol. 12 (3) (2017) 194–206, https://doi.org/10.1038/nnano.2017.16.
[10] Z. Hu, J. Li, X. Zhang, Y. Zhu, Strategies to improve the performance of Li metal anode for rechargeable batteries, Front. Chem. 8 (2020) 409, https://doi.org/10.3389/fchem.2020.00409.
[11] S.A. Han, H. Qutaish, M.-S. Park, J. Moon, J.H. Kim, Strategic approaches to the dendritic growth and interfacial reaction of lithium metal anode, Chem. Asian J. 16 (24) (2021) 4010–4017, https://doi.org/10.1002/asia.202101108.
[12] X. Yan, L. Lin, Q. Chen, Q. Xie, B. Qu, L. Wang, D.-L. Peng, Multifunctional roles of carbon-based hosts for Li-metal anodes: a review, Carbon Energy 3 (2) (2021) 303–329, https://doi.org/10.1002/cey2.95.
[13] B. Liu, J.-G. Zhang, W. Xu, Advancing lithium metal batteries, Joule 2 (2018) 833–845, https://doi.org/10.1016/j.joule.2018.03.008.
[14] J.-F. Ding, R. Xu, X.-X. Ma, Y. Xiao, Y.-X. Yao, C. Yan, J.-Q. Huang, Quantificationof the dynamic interface evolution in high-efficiency working Li-metal batteries, Angew. Chem. Int. Ed. 61 (2022), e202115602, https://doi.org/10.1002/anie.202115602.
[15] Q. Wang, B. Liu, Y. Shen, J. Wu, Z. Zhao, C. Zhong, W. Hu, Confronting the challenges in lithium anodes for lithium metal batteries, Adv. Sci. 8 (2021) 2101111, https://doi.org/10.1002/advs.202101111.
[16] J. Wang, B. Ge, H. Li, M. Yang, J. Wang, D. Liu, C. Fernandez, X. Chen, Q. Peng, Challenges and progresses of lithium-metal batteries, Chem. Eng. J. 420 (2021), 129739, https://doi.org/10.1016/j.cej.2021.129739.
[17] H. Zhang, L. Zhou, X. Du, J. Zhang, S. Tian, T. Liu, J. Zhang, S. Hu, W. Song, X. Zhou, G. Cui, Cyanoethyl cellulose-based eutectogel electrolyte enabling high-voltage-tolerant and ion-conductive solid-state lithium metal batteries, Carbon Energy 4 (2022) 1093–1106, https://doi.org/10.1002/cey2.227.
[18] J. Yang, X. Li, K. Qu, Y. Wang, K. Shen, C. Jiang, B. Yu, P. Luo, Z. Li, M. Chen, B. Guo, M. Wang, J. Chen, Z. Ma, Y. Huang, Z. Yang, P. Liu, R. Huang, X. Ren, D. Mitlin, Concentrated ternary ether electrolyte allows for stable cycling of a lithium metal battery with commercial mass loading high-nickel NMC and thin anodes, Carbon Energy 5 (2023) e275, https://doi.org/10.1002/cey2.275.
[19] Z.A. Ghazi, Z. Sun, C. Sun, F. Qi, B. An, F. Li, H.-M. Cheng, Key aspects of lithium metal anodes for lithium metal batteries, Small 15 (32) (2019) 1900687, https://doi.org/10.1002/smll.201900687.

[20] H. Ye, Y. Zhang, Y.-X. Yin, F.-F. Cao, Y.-G. Guo, An outlook on low-volume-change lithium metal anodes for long-life batteries, ACS Cent. Sci. 6 (5) (2020) 661–671, https://doi.org/10.1021/acscentsci.0c00351.
[21] Q. Lu, Y. Jie, X. Meng, A. Omar, D. Mikhailova, R. Cao, S. Jiao, Y. Lu, Y. Xu, Carbon materials for stable Li metal anodes: challenges, solutions, and outlook, Carbon Energy 3 (6) (2021) 957–975, https://doi.org/10.1002/cey2.147.
[22] Y. Hyeon, J. Lee, H. Qutaish, S.A. Han, S.H. Choi, S.W. Moon, M.-S. Park, D. Whang, J.H. Kim, Lithium metal storage in zeolitic imidazolate framework derived nanoarchitectures, Energy Storage Mater. 33 (2020) 95–107, https://doi.org/10.1016/j.ensm.2020.07.015.
[23] J.I. Jung, S. Park, S. Ha, S.Y. Cho, H.-J. Jin, Y.S. Yun, Effects of nanopores and sulfur doping on hierarchicallybunched carbon fibers to protect lithium metal anode, Carbon Energy. 3 (5) (2021) 784–794, https://doi.org/10.1002/cey2.128.
[24] L. Xiao, Z. Zeng, X. Liu, Y. Fang, X. Jiang, Y. Shao, L. Zhuang, X. Ai, H. Yang, Y. Cao, J. Liu, Stable li metal anode with "ion–solvent-coordinated" nonflammable electrolyte for safe li metal batteries, ACS Energy Lett. 4 (2) (2019) 483–488, https://doi.org/10.1021/acsenergylett.8b02527.
[25] C. Niu, H. Pan, W. Xu, J. Xiao, J. -G. Zhang, L. Luo, C. Wang , D. Mei,, J. Meng, X. Wang, Ziang Liu, L. Mai, J. Liu, Self-smoothing anode for achieving high-energy lithium metal batteries under realistic conditions. Nat Nanotechnol. 14(6) (2019) 594-601, https://doi.org/10.1038/s41565-019-0427-9.
[26] K.-C. Pu, X. Zhang, X.-L. Qu, J.-J. Hu, H.-W. Li, M.-X. Gao, H.-G. Pan, Y.-F. Liu, Recently developed strategies to restrain dendrite growth of Li metal anodes for rechargeable batteries, Rare Met. 39 (6) (2020) 616–635, https://doi.org/10.1007/s12598-020-01432-2.
[27] A. Ramasubramanian, V. Yurkiv, T. Foroozan, M. Ragone, R. Shahbazian-Yassar, F. Mashayek, Stability of solid-electrolyte interphase (SEI) on the lithium metal surface in lithium metal batteries (LMBs), ACS Appl. Energy Mater. 3 (11) (2020) 10560–10567, https://doi.org/10.1021/acsaem.0c01605.
[28] H. Adenusi, G.A. Chass, S. Passerini, K.V. Tian, G. Chen, Lithium Batteries and the solid electrolyte interphase (SEI)-progress and outlook, Adv. Energy Mater. 13 (2023) 2203307, https://doi.org/10.1002/aenm.202203307.
[29] W. Cao, J. Lu, K. Zhou, G. Sun, J. Zheng, Z. Geng, H. Li, Organic-inorganic composite SEI for a stable Li metal anode by in-situ polymerization, Nano Energy 95 (2022), 106983, https://doi.org/10.1016/j.nanoen.2022.106983.
[30] Z. Wang, L.-P. Hou, Z. Li, J.-L. Liang, M.-Y. Zhou, C.-Z. Zhao, X. Zeng, B.-Q. Li, A. Chen, X.-Q. Zhang, P. Dong, Y. Zhang, J.-Q. Huang, Q. Zhang, Highly soluble organic nitrate additives for practical lithium metal batteries, Carbon Energy 5 (1) (2023) e283, https://doi.org/10.1002/cey2.283.
[31] N. Piao, S. Liu, B. Zhang, X. Ji, X. Fan, L. Wang, P.-F. Wang, T. Jin, S.-C. Liou, H. Yang, J. Jiang, K. Xu, M.A. Schroeder, X. He, C. Wang, Lithium Metal batteries enabled by synergetic additives in commercial carbonate electrolytes, ACS Energy Lett. 6 (5) (2021) 1839–1848, https://doi.org/10.1021/acsenergylett.1c00365.
[32] Y. Zhong, Y. Chen, Y. Cheng, Q. Fan, H. Zhao, H. Shao, Y. Lai, Z. Shi, X. Ke, Z. Guo, Li Alginate-based artificial SEI layer for stable lithium metal anodes, ACS Appl. Mater. Interfaces 11 (41) (2019) 37726–37731, https://doi.org/10.1021/acsami.9b12634.
[33] Z. Yu, Y. Cui, Z. Bao, Design principles of artificial solid electrolyte interphases for lithium-metal anodes, Cell Rep. Phys. Sci. 1 (7) (2020), 100119, https://doi.org/10.1016/j.xcrp.2020.100119.
[34] H. Liu, J. Di, P. Wang, R. Gao, H. Tian, P. Ren, Q. Yuan, W. Huang, R. Liu, Q. Liu, M. Feng, A novel design of 3D carbon host for stable lithium metal anode, Carbon Energy 4 (4) (2023) 654–664, https://doi.org/10.1002/cey2.193.
[35] D. Li, B. Chen, H. Hu, W.-Y. Lai, Constructing 3D porous current collectors for stable and dendrite-free lithium metal anodes, Adv. Sustainable Syst. 6 (5) (2022) 202200010, https://doi.org/10.1002/adsu.202200010.
[36] S.A. Han, H. Qutaish, J.-W. Lee, M.-S. Park, J.H. Kim, Metal-organic framework derived porous structures towards lithium rechargeable batteries, EcoMat. 5 (2) (2023), e12283, https://doi.org/10.1002/eom2.12283.
[37] J. Kim, J. Lee, J. Yun, S.H. Choi, S.A. Han, J. Moon, J.H. Kim, J.-W. Lee, M.-S. Park, Functionality of dual-phase lithium storage in a porous carbon host for lithium-metal anode, Adv. Funct. Mater. 30 (15) (2020) 1910538, https://doi.org/10.1002/adfm.201910538.
[38] S.H. Choi, Y. Hyeon, H.R. Shin, G.H. Eom, H.T.T. Pham, D. Whang, S.Y. Kim, J.-W. Lee, J.H. Kim, M.-S. Park, Critical role of surface craters for improving the reversibility of li metal storage in porous carbon frameworks, Nano Energy 88 (2021), 106243, https://doi.org/10.1016/j.nanoen.2021.106243.
[39] G.H. Eom, S.A. Han, J.H. Suh, J.H. Kim, M.-S. Park, Enriched cavities to ZIF-8-derived porous carbon for reversible metallic lithium storage, ACS Appl. Energy Mater. 4 (12) (2021) 14520–14525, https://doi.org/10.1021/acsaem.1c03168.
[40] T. Lyu, F. Luo, D. Wang, L. Bu, L. Tao, Z. Zheng, Carbon/lithium composite anode for advanced lithium metal batteries: design, progress, in situ characterization, and perspectives, Adv. Energy Mater. 12 (36) (2022) 2201493, https://doi.org/10.1002/aenm.202201493.
[41] Y. Liu, Y. Zhai, Y. Xia, W. Li, D. Zhao, Recent progress of porous materials in lithium-metal batteries, Small Struct. 2 (5) (2021) 2000118, https://doi.org/10.1002/sstr.202000118.
[42] H. Qutaish, J.H. Suh, S.A. Han, S. Kim, M.-S. Park, J.H. Kim, Regulation of ionic conductivity and lithium affinity of porous carbon framework in Li metal batteries through oxidized nitrogen groups, Appl. Surf. Sci. 605 (2022), 154757, https://doi.org/10.1016/j.apsusc.2022.154757.
[43] S. Fang, L. Shen, S. Li, G.-T. Kim, D. Bresser, H. Zhang, X. Zhang, J. Maier, S. Passerini, Alloying reaction confinement enables high-capacity and stable anodes for lithium-ion batteries, ACS Nano 13 (8) (2019) 9511–9519, https://doi.org/10.1021/acsnano.9b04495.
[44] Y. Fang, S.L. Zhang, Z.-P. Wu, D. Luan, X.W. Lou, A highly stable lithium metal anode enabled by Ag nanoparticle–embedded nitrogen-doped carbon macroporous fibers, Sci. Adv. 7 (21) (2021) eabg3626, https://doi.org/10.1126/sciadv.abg3626.
[45] Y. Fan, J. Liao, D. Luo, Y. Huang, F. Sun, J. Nan, In situ formation of a lithiophilic surface on 3D current collectors to regulate lithium nucleation and growth for dendrite-free lithium metal anodes, Chem. Eng. J. 452 (2) (2023), 139903, https://doi.org/10.1016/j.cej.2022.139903.
[46] K. Yan, Z. Lu, H.-W. Lee, F. Xiong, P.-C. Hsu, Y. Li, J. Zhao, S. Chu, Y. Cui, Selective deposition and stable encapsulation of lithium through heterogeneous seeded growth, Nat. Energy 1 (3) (2016) 1–8, https://doi.org/10.1038/nenergy.2016.10.
[47] J. Wu, X. Chen, W. Fan, X. Li, Y.-W. Mai, Y. Chen, Rationally designed alloy phases for highly reversible alkali metal batteries, Energy Storage Mater. 48 (2022) 223–243, https://doi.org/10.1016/j.ensm.2022.03.018.
[48] H.R. Shin, J. Yun, G.H. Eom, J. Moon, J.H. Kim, M.-S. Park, J.-W. Lee, S.X. Dou, Mechanistic and nanoarchitectonics insight into Li–host interactions in carbon hosts for reversible Li metal storage, Nano Energy 95 (2022), 106999, https://doi.org/10.1016/j.nanoen.2022.106999.
[49] B.T. Heligman, A. Manthiram, Elemental foil anodes for lithium-ion batteries, ACS Energy Lett. 6 (8) (2021) 2666–2672, https://doi.org/10.1021/acsenergylett.1c01145.
[50] Y. Zhong, B. Li, S. Li, S. Xu, Z. Pan, Q. Huang, L. Xing, C. Wang, W. Li, Bi nanoparticles anchored in N-doped porous carbon as anode of high energy density lithium ion battery, Nano-Micro Lett. 10 (4) (2018) 56, https://doi.org/10.1007/s40820-018-0209-1.
[51] T. Chen, F. Meng, Z. Zhang, J. Liang, Y. Hu, W. Kong, X.L. Zhang, Z. Jin, Stabilizing lithium metal anode by molecular beam epitaxy grown uniform and ultrathin bismuth film, Nano Energy 76 (2020), 105068, https://doi.org/10.1016/j.nanoen.2020.105068.
[52] W. Hong, P. Ge, Y. Jiang, L. Yang, Y. Tian, G. Zou, X. Cao, H. Hou, X. Ji, Yolk–shell-structured bismuth@ N-doped carbon anode for lithium-ion battery with high volumetric capacity, ACS Appl. Mater. Interfaces 11 (11) (2019) 10829–10840, https://doi.org/10.1021/acsami.8b20477.
[53] W. Choi, H.-C. Shin, J.M. Kim, J.-Y. Choi, W.-S. Yoon, Modeling and applications of electrochemical impedance spectroscopy (EIS) for lithium-ion batteries, J. Electrochem. Sci. Technol. 11 (1) (2020) 1–13, https://doi.org/10.33961/jecst.2019.00528.
[54] J. Yan, M. Liu, N. Deng, L. Wang, A. Sylvestre, W. Kang, Y. Zhao, Flexible MnO nanoparticle-anchored N-doped porous carbon nanofiber interlayers for superior performance lithium metal anodes, Nanoscale Adv. 3 (2021) 1136–1147, https://doi.org/10.1039/D0NA00690D.
[55] C. Jin, O. Sheng, J. Luo, H. Yuan, C. Fang, W. Zhang, H. Huang, Y. Gan, Y. Xia, C. Liang, J. Zhang, X. Tao, 3D lithium metal embedded within lithiophilic porous matrix for stable lithium metal batteries, Nano Energy 37 (2017) 177–186, https://doi.org/10.1016/j.nanoen.2017.05.015.
[56] T. Kim, W. Choi, H.-C. Shin, J.-Y. Choi, J.M. Kim, M.-S. Park, W.-S. Yoon, Applications of voltammetry in lithium ion battery research, J. Electrochem. Sci. Technol. 11 (1) (2020) 14–25, https://doi.org/10.33961/jecst.2019.00619.